

A Hydrazine–Water Galvanic Cell-Inspired Self-Powered High-Rate Hydrogen Production via Overall Hydrazine Electrosplitting

Linjie Zhang, Man Li, Chen Sun, Hsiao-Tsu Wang, Yi Xiao, Ke Ma, Yimeng Cai, Cheng-You Lee, Yu-Cheng Shao, Chia-Hsin Wang, Shuwen Zhao, Hirofumi Ishii, Nozomu Hiraoka, Xiuyun Wang, Chih-Wen Pao, and Lili Han*

Exploring advanced electrolysis techniques for attaining scene-adaptive and on-site green H₂ production is an imperative matter of utmost practical significance but grand challenge remains. Herein, drawn inspiration from a spontaneous hydrazine–H₂O galvanic cell configured on a low-valence Ru single atoms-loaded Mo₂C electrode (Ru_{SA}/v-Mo₂C), an alternative H₂ energy solution utilizing self-powered electrochemical hydrazine splitting (N₂H₄ → 2H₂ + N₂) instead of the stereotyped electricity-consumed water splitting for green H₂ production is proposed. This solution highlights a pH-decoupled hydrazine–H₂O primary battery with notable open-circuit voltage of 1.37 V and energy density up to 358 Wh g_{N₂H₄}⁻¹, which powerfully propels an alkaline hydrazine splitting cell, leading to bilateral H₂ harvest with a remarkable rate of 18 mol h⁻¹ m⁻², i.e., 403.2 L h⁻¹ m⁻², setting a new record for the self-sustaining electricity-powered H₂ production systems. The success of Ru_{SA}/v-Mo₂C for this solution is further decoded by tandem theoretical and *in situ* spectroscopic studies, cross-verifying a Ru–Mo dual-site synergy in streamlining the overall energy barriers, thereby enhancing the kinetics of electrode reactions. This pioneering work, showcasing electrochemical H₂ production free from both external energy and feedstock inputs, opens up a new horizon on way of the ultimate H₂ energy solution.

natural scarcity and reliance on fossil fuel extraction.^[1] The shift toward green H₂ extraction via water electrolysis powered by renewable energy sources, such as hydro, wind, and solar, represents a promising path forward.^[2] Despite remarkable progress, severe fundamental challenges persist, including the needs for efficient electrodes, pH-adaptive electrocatalysts, and solutions to kinetic imbalances between the cathodic hydrogen evolution reaction (HER) and oxygen evolution reaction (OER).^[3] Besides the sluggish kinetics, OER raises safety concerns due to the risk of explosive H₂/O₂ mixture from gas crossover.^[4] More importantly, integrating scale-up water electrolysis systems with intermittent renewable sources while maintaining efficient and stable operation is formidable. To enable green H₂ a part of our energy mix, it substantiates significant infrastructural investments, let alone the costly H₂ storage and transport, which currently even take more energy than that H₂ can provide.^[5] Therefore, a shift toward more favorable electrochemical extraction and utilization of H₂ needs to be innovated.

Recent years have witnessed a prevalence in replacing OER with the thermodynamically more favorable electrocatalytic oxidation of organic small molecules for coupling HER.^[6] This

1. Introduction

Hydrogen (H₂) energy is acclaimed as a cornerstone for a decarbonized future, yet its sustainability is compromised by

L. Zhang, M. Li, C. Sun, Y. Xiao, K. Ma, Y. Cai, S. Zhao, L. Han
 State Key Laboratory of Structural Chemistry
 Fujian Institute of Research on the Structure of Matter
 Chinese Academy of Sciences
 Fuzhou 350002, China
 E-mail: llhan@fjirsm.ac.cn

L. Zhang, M. Li, C. Sun, S. Zhao, L. Han
 School of Chemical Sciences
 University of Chinese Academy of Sciences
 Beijing 101408, China

H.-T. Wang, C.-Y. Lee, C.-W. Pao
 Department of Physics
 Tamkang University
 New Taipei City 251301, Taiwan
 Y.-C. Shao, C.-H. Wang, H. Ishii, N. Hiraoka
 National Synchrotron Radiation Research Center
 Hsinchu 30076, Taiwan
 X. Wang
 National Engineering Research Center of Chemical Fertilizer Catalyst
 Fuzhou University
 Fuzhou 350002, China

 The ORCID identification number(s) for the author(s) of this article can be found under <https://doi.org/10.1002/adfm.202420163>

DOI: 10.1002/adfm.202420163

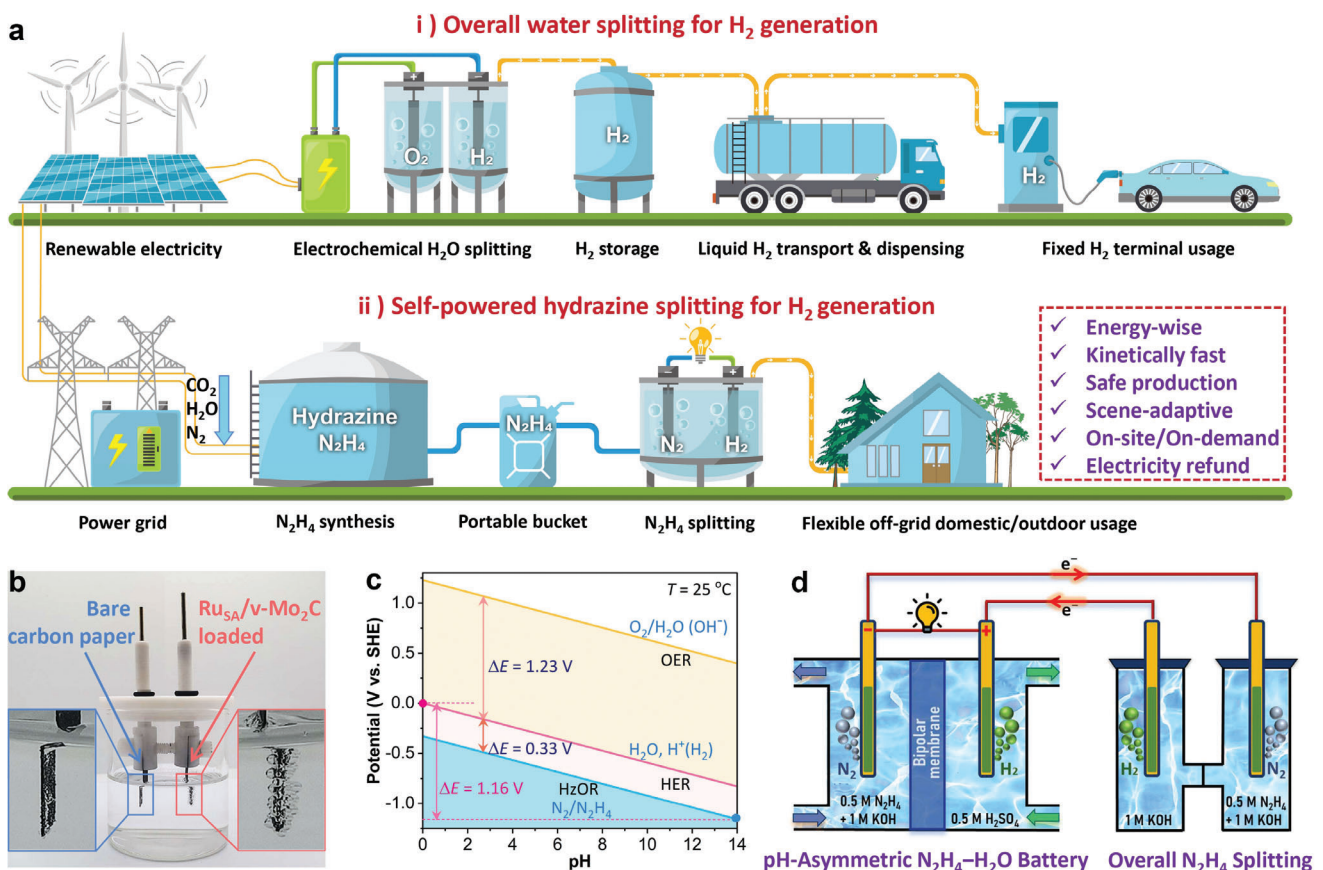


Figure 1. Proposed hydrazine splitting route for H_2 production and schematic working principle of the conceptual hydrazine– H_2O battery. **a)** Workflow comparison of the overall water splitting and hydrazine splitting for H_2 production and usage. **b)** Digital photo demonstrating the spontaneous HzOR/HER galvanic cell with massive bubbles adhered on the Ru_{SA}/v-Mo₂C-loaded carbon paper electrode in a 1 M KOH and 0.5 M N_2H_4 electrolyte. **c)** E-pH Pourbaix diagram for HzOR, HER, and OER. **d)** Schematic illustrating the hybrid self-powered hydrazine splitting system for bilateral H_2 production.

approach extracts H_2 from organics splitting instead of water splitting, thus bypassing the drawbacks associated with OER, leading to more energy-saving, faster and safer H_2 production. Of particular allure is the H_2 extraction from hydrazine splitting ($N_2H_4 \rightarrow 2H_2 + N_2$), due to the significantly faster kinetics and lower thermodynamic equilibrium potential of hydrazine oxidation reaction (HzOR, $E^\circ_{RHE} = -0.33$ V) compared to OER ($E^\circ_{RHE} = 1.23$ V),^[7] which offers great potential for reducing the electricity consumption and cost. Notably, it has been reported that an ampere-level hydrazine splitting can be achieved at a voltage as low as 0.69 V.^[8] Besides, the only byproduct is N_2 , thereby ensuring a safe operation. Moreover, hydrazine serves as important industrial chemical and fuel, its extensive use results in the generation of substantial quantities of hazardous hydrazine wastewater. Consequently, hydrazine splitting technology presents the dual benefit of producing H_2 while eliminating the associated hazards of hydrazine, thereby further enhancing its economic viability. In hydrazine splitting, the liquid hydrazine acts as a hydrogen carrier (12.5 wt% H), which is much higher in volumetric energy density and more feasible to store and transport than H_2 . This makes hydrazine an ideal H_2 energy mediator, enabling it a surrogate to glean the intermittent renewable electricity for in-

tegration into the power grid (Figure 1a). Consequently, electrochemical hydrazine splitting offers a transitional H_2 energy solution, facilitating on-site and on-demand H_2 usage mode for various portable electronics and mobile vehicles. However, a critical hurdle in realizing this scenario is driving the hydrazine splitting to release stored H_2 independently of external power sources. Currently, there are some so-called self-powered hydrazine splitting hybrid systems using powers from direct hydrazine fuel cells (DHFCs).^[9] Yet they demand additional use of air/ O_2 or H_2O_2 , which not only limits the on-site/on-demand H_2 usage especially in outdoors or anaerobic environments but also increases the complexity and cost for H_2 production. Therefore, there exists an urgency to develop a real self-powered hydrazine splitting system driven by internally generated electricity with hydrazine as the sole consumable.

Virtually, when looking into the DHFCs characterized by the redox pair of anodic HzOR and cathodic O_2 reduction reaction (ORR), if replacing the ORR with H_2O reduction (HER), it will be possible to mimic DHFCs to formulate a likewise hydrazine– H_2O cell reliant solely on hydrazine consumption. While the thermodynamic equilibrium potential of HzOR ($E^\circ_{RHE} = -0.33$ V) happens to be lower than that of HER ($E^\circ_{RHE} = 0$ V),^[7b]

indicating the spontaneity of the proposed hydrazine–H₂O cell,^[10] thereby meeting the autogenic electricity criterion. However, to accomplish this goal, the utilization of highly efficient electrocatalysts for both HzOR and HER is crucial to minimizing the potential polarization. Ru, a member of the Pt-group metals with only one-quarter the price of Pt, has attracted considerable attention in both HER and HzOR electrocatalysis.^[11] However, the relatively strong Ru–H and Ru–N₂H_x binding strengths lead to yet inferior performance of Ru in these reactions compared to that of Pt.^[12] Besides, conventional Ru nanoparticles suffer from low atomic utilization, susceptibility to dissolution in alkaline electrolytes, and easy oxidation under high potentials, which further limit their catalytic efficacy.^[13] To mitigate these challenges, reducing Ru nanoparticles to single atoms (SAs) and stabilizing them on supports that exhibit strong electronic metal-support interaction (EMSI) would be a preferable strategy.^[14] While the current Ru SAs typically exist in a high oxidation state and are supported on carbonous materials with relatively weak EMSI, which limits their ability to sustain high activity and efficiently facilitate electronic synergy necessary for addressing the diverse intermediates adsorption throughout various reaction steps.^[15] Instead, Mo₂C is recognized for its strong electron donating capacity, high electric conductivity, and robust electrochemical stability, making it an appealing alternative for supporting Ru SAs with strong EMSI, and effectively regulating their electronic structures by generating metal–metal interactions, thereby optimizing the binding strengths of reaction intermediates.^[16] Furthermore, the high oxophilicity of Mo could favor the OH binding simultaneously, which has been shown to play a crucial role in improving the sluggish kinetics of water dissociation in alkaline HER,^[17] and is also expected to boost the dehydrogenation kinetics of N₂H_x intermediates during HzOR. Despite these advantages, the existing Ru SAs on noncarbon supports generally present low loading levels, highlighting the urgent need for more efficient synthetic methodology.

Herein, we have developed a low-valence Ru single atom catalyst loaded on Mo₂C nanobelts (Ru_{SA}/v-Mo₂C), which successfully facilitates the spontaneous hydrazine splitting in a 1 M KOH aqueous solution containing 0.5 M hydrazine without external electricity (Figure 1b; and Movie S1, Supporting Information), due to its excellent HER/HzOR bifunctionality underpinning a galvanic-type hydrazine–H₂O cell configured on a single electrode.^[18] Inspired upon the insights gained from this galvanic cell, a high-voltage hydrazine–H₂O battery with pH-decoupled electrolytes has been exquisitely designed to output the electricity. As shown in Figure 1c, according to the E–pH Pourbaix diagram for HzOR and HER profiled using the Nernst equation, the theoretical voltage window of this battery can be expanded to 1.16 V by coupling acidic HER in an electrolyte of pH = 0 and alkaline HzOR in an electrolyte of pH = 14 (for calculation details, see the Supporting Information). Hereof, a hybrid self-powered hydrazine splitting system for H₂ production has been established by connecting the hydrazine–H₂O battery to an alkaline hydrazine splitting electrolyzer using solely the Ru_{SA}/v-Mo₂C electrode and hydrazine consumable (Figure 1d). Notably, both the battery and electrolyzer involve hydrazine splitting, thus empowering a bilateral H₂ harvest with an ultrahigh rate of 18 mol h⁻¹ m⁻², exceeding all other reported self-powered H₂ production system, and with far-lower cost and higher scene

adaptability. This innovative design outlined herein stands as a paradigmatic showcase for the route toward a sustainable and flexible hydrogen future.

2. Results and Discussion

2.1. Synthesis and Characterizations

The bifunctional HER/HzOR electrocatalyst, Ru_{SA}/v-Mo₂C, was synthesized by a vacancy-trapping synthetic strategy schematically illustrated in Figure 2a. First, Zn-doped MoO₃ nanobelts were prepared hydrothermally, and subsequently converted to N-doped and cationic vacancies-enriched Mo₂C (denoted as v-Mo₂C) by a high-temperature gas–solid reaction using urea as the carbon source (Figures S1 and S2, Supporting Information). In this process, the thermal decomposition of urea generates substantial CO_x and NH₃ gases,^[19] which simultaneously facilitates metal carbonization and the incorporation of N dopants into the carbide. Additionally, it promotes the vaporization of Zn from the carbide, resulting in the abundant formation of Moⁿ⁺ vacancies (V_{Mo}ⁿ⁺). Subsequently, the v-Mo₂C nanobelts underwent thorough wet-chemical impregnation with RuCl₃, with Ru³⁺ ions being trapped by the cationic V_{Mo}ⁿ⁺. Finally, after thermal annealing under an Ar atmosphere, the formation of low-valence Ru single atoms supported on v-Mo₂C (Ru_{SA}/v-Mo₂C) was achieved.

Transmission electron microscopy (TEM) revealed the similar nanobelt morphology of Ru_{SA}/v-Mo₂C inherited from their parent Zn-doped MoO₃ nanobelts (Figure 2b). Unlike the smooth Zn-doped MoO₃ nanobelts, Ru_{SA}/v-Mo₂C nanobelts exhibit an enhanced porous character due to the assembly of secondary nanoparticles, as vividly visualized in their 3D reconstruction by TEM electron tomography (Figure 2c; and Movie S2, Supporting Information). Moreover, beyond the Mo and N signals, a uniform Ru signal distribution across the Ru_{SA}/v-Mo₂C nanobelts without any agglomeration was discerned in elemental mappings compared to v-Mo₂C (Figure 2d,e). Microscopic atomic structural analysis using subatomic resolution high-angle annular dark field scanning TEM (HAADF-STEM) confirmed the formation of Ru SAs in Ru_{SA}/v-Mo₂C, as evidenced by isolated atoms with a slightly brighter contrast highlighted within circles (Figure 2f; and Figure S3, Supporting Information).^[20] Conversely, v-Mo₂C exhibits a significant presence of atomic V_{Mo}ⁿ⁺ (Figure 2g). This contrasting observation suggests Ru SAs precisely occupied the V_{Mo}ⁿ⁺ sites within v-Mo₂C during the vacancy-trapping synthetic process and successfully integrated into the Mo₂C lattice after the reaction. Visual representations of atomic arrangement models mimicking the lattices of Ru_{SA}/v-Mo₂C and v-Mo₂C are depicted in Figure 2h,i. Besides, the presence of individual Ru SA in Ru_{SA}/v-Mo₂C and V_{Mo}ⁿ⁺ in v-Mo₂C is substantiated by the heterogeneous atomic intensity line scanning profiles shown in Figure 2j,k.

The similar powder X-ray diffraction (XRD) patterns of Ru_{SA}/v-Mo₂C and v-Mo₂C reveal a same hexagonal β-Mo₂C phase for both samples (Figure 2l), and no diffraction peaks indexing to Ru species were detected, further affirming the existence of Ru SAs in Ru_{SA}/v-Mo₂C. Besides, electron paramagnetic resonance (EPR) unveils an identical signal at g = 2.0023 characteristic of Moⁿ⁺ for v-Mo₂C and Ru_{SA}/v-Mo₂C (Figure 2m),^[21] indicating the presence of V_{Mo}ⁿ⁺ in both samples. However, a notable

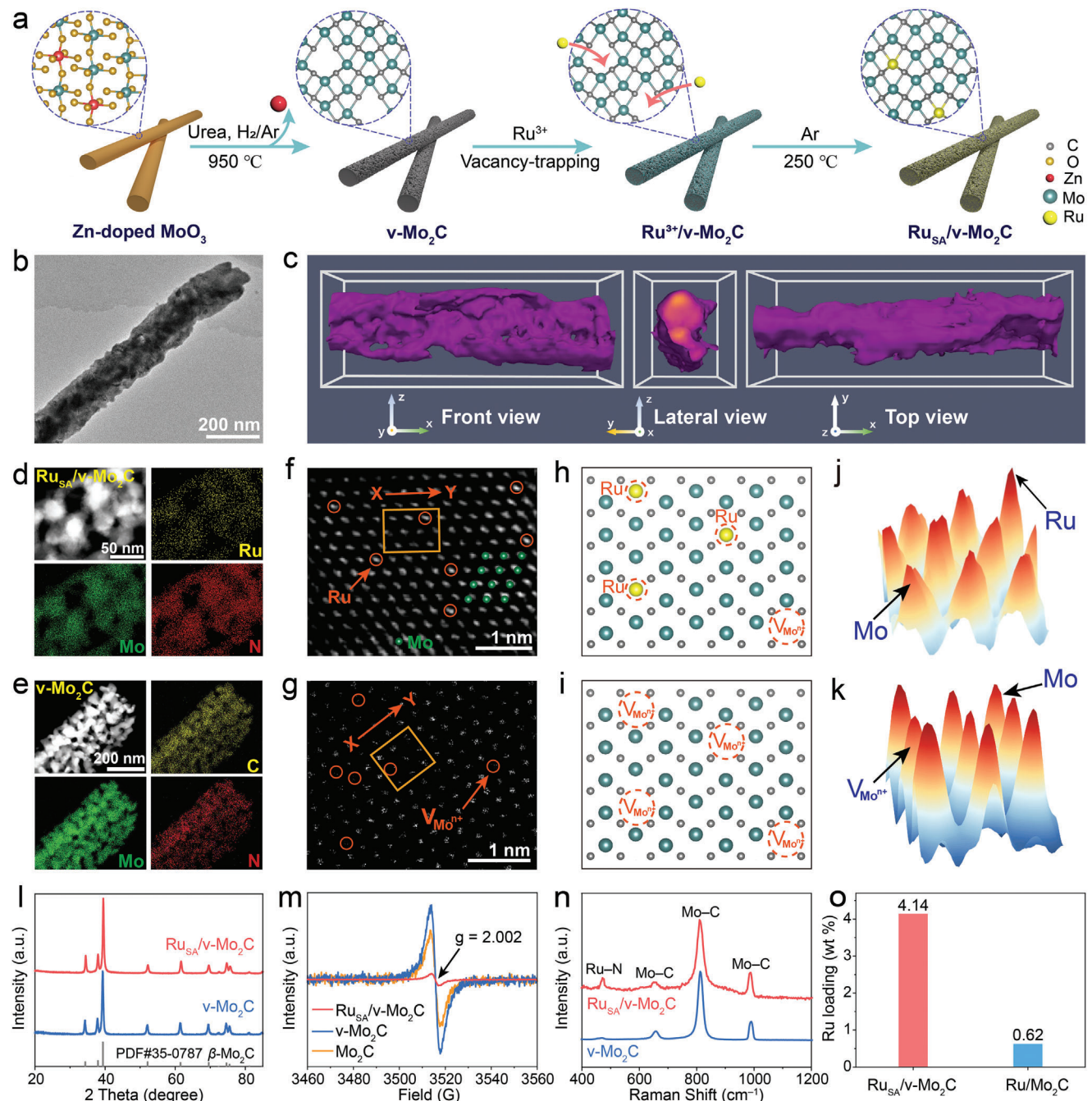


Figure 2. Synthesis and structural characterizations. a) Schematic synthesis, b) TEM image, and c) 3D reconstruction of Ru_{SA}/v-Mo₂C. STEM-EDS mappings of d) Ru_{SA}/v-Mo₂C and e) v-Mo₂C. HAADF-STEM images of f) Ru_{SA}/v-Mo₂C and g) v-Mo₂C. Schematic lattice atom arrangement on β-Mo₂C (101) with trapped Ru SAs for h) Ru_{SA}/v-Mo₂C and Moⁿ⁺ vacancies for i) v-Mo₂C. j,k) Intensity profiles of the regions marked by orange boxes in (f) and (g) along the line X-Y, respectively. l) XRD patterns. m) EPR spectra. n) Raman spectra. o) Ru-loading comparison between Ru_{SA}/v-Mo₂C and Ru/Mo₂C.

decrease in the intensity of V_{Mo}ⁿ⁺ EPR signal was observed for Ru_{SA}/v-Mo₂C compared to v-Mo₂C, suggesting a reduction of V_{Mo}ⁿ⁺ concentration after the formation of Ru SAs. These results confirm that Ru SA occupies the V_{Mo}ⁿ⁺ site, thus justifying the cationic vacancies-guided single-atom trapping synthetic mechanism for Ru_{SA}/v-Mo₂C. Moreover, Raman spectra of Ru_{SA}/v-Mo₂C and v-Mo₂C exhibit distinct characteristic peaks of Mo₂C

at 652, 812, and 995 cm⁻¹ (Figure 2n), assigning to the stretching mode of Mo-C.^[22] Notably, a weak peak at 474 cm⁻¹ was observed in Ru_{SA}/v-Mo₂C, which can be reasoned to the E_g vibration mode of Ru-N,^[23] suggesting N coordination in the first shell of Ru SAs. Furthermore, inductively coupled plasma optical emission spectrometry (ICP-OES) determined a remarkably higher Ru loading of 4.14 wt% in Ru_{SA}/v-Mo₂C compared to only

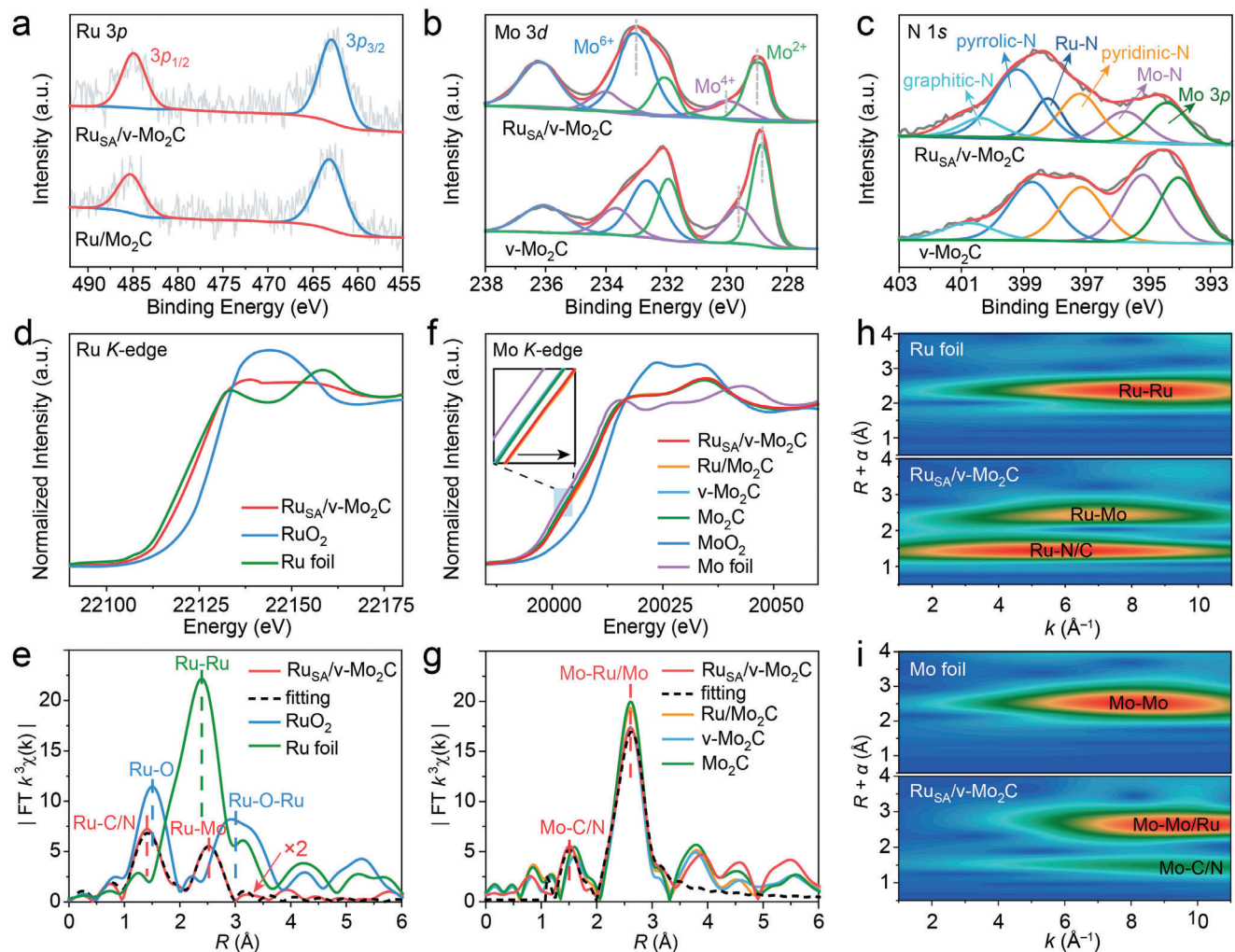


Figure 3. Electronic structure and local coordination environment analyses. a) Ru 3p, b) Mo 3d, and c) N 1s XPS spectra of $\text{Ru}_{\text{SA}}/\text{v-Mo}_2\text{C}$ and reference samples. d,e) Ru K-edge and f,g) Mo K-edge XANES and FT-EXAFS spectra of $\text{Ru}_{\text{SA}}/\text{v-Mo}_2\text{C}$ and reference samples. h) Ru K-edge and i) Mo K-edge WT-EXAFS spectra of $\text{Ru}_{\text{SA}}/\text{v-Mo}_2\text{C}$.

0.62 wt% Ru loading in $\text{V}_{\text{Mo}}^{n+}$ -free Mo_2C substrate ($\text{Ru}/\text{Mo}_2\text{C}$) (Figure 2o; and Figures S4–S5, Supporting Information), as well as majority of the reported Ru SAs loaded on various Mo_2C substrates, thus highlighting the efficacy of the developed synthetic route for anchoring single atoms through vacancy-trapping.

2.2. Electronic and Local Atomic Structural Analyses

The surface elemental valence and electronic interaction between Ru SAs and Mo_2C support were investigated through X-ray photoelectron spectroscopy (XPS) (Figure S6, Supporting Information). High-resolution Ru 3p XPS of $\text{Ru}_{\text{SA}}/\text{v-Mo}_2\text{C}$ reveals peaks at binding energies of 485 and 463 eV for the $3p_{1/2}$ and $3p_{3/2}$ orbits (Figure 3a), respectively. These peaks exhibit a slight blueshift compared with those observed for $\text{Ru}/\text{Mo}_2\text{C}$ and the Ru metals,^[24] consistent with the Ru 3d XPS analysis (Figure S7, Supporting Information), indicating a minor oxidation of the Ru SAs with a low-valence state. The high-resolution Mo 3d XPS

of $\text{Ru}_{\text{SA}}/\text{v-Mo}_2\text{C}$ can be deconvoluted into three doublets corresponding to Mo^{2+} (229.0 and 232.1 eV) and Mo^{4+} (230.0 and 234.0 eV) for Mo_2C , and Mo^{6+} (233 and 236.2 eV) for MoO_x oxides arising from inevitable partial surface oxidation of Mo_2C upon exposure to air (Figure 3b), consistent with prior XPS analyses for $\beta\text{-Mo}_2\text{C}$.^[21,25] In comparison to $\text{v-Mo}_2\text{C}$, the binding energies of Mo^{2+} and Mo^{4+} 3d peaks of $\text{Ru}_{\text{SA}}/\text{v-Mo}_2\text{C}$ exhibit an increase of ≈ 0.25 eV, alongside a 3.84% rise in the Mo^{6+} proportion from 33.92% to 37.76%. This suggests a significant electron transfer from the Mo_2C support to the Ru SAs. Such behavior can be attributed to the unique metalloid characteristics of Mo_2C , enabling it to act as an effective electron donor to reduce the valence state of Ru SAs and facilitate metal–metal interactions,^[16,26] which are beneficial for the stabilization and activity enhancement of Ru SAs. The N 1s XPS of $\text{Ru}_{\text{SA}}/\text{v-Mo}_2\text{C}$ unveils the presence of typical graphitic N, pyrrolic N, pyridinic N, and Mo–N (395.8 eV) similar to that of $\text{v-Mo}_2\text{C}$ (Figure 3c).^[27] Additionally, an extra peak at 396.1 eV corresponding to the Ru–N bond was observed,^[28] confirming the presence of N ligand in the first

coordination shell of Ru SAs. To delve into the local electronic structure and coordination environment within $\text{Ru}_{\text{SA}}/\text{v-Mo}_2\text{C}$, synchrotron X-ray absorption study was conducted for both Ru and Mo elements. As depicted in Figure 3d, the Ru K-edge X-ray absorption near edge structure (XANES) spectrum of $\text{Ru}_{\text{SA}}/\text{v-Mo}_2\text{C}$ is close to that of Ru foil and the white line peak intensity is significantly lower than that of RuO_2 , indicating a low oxidation state of Ru SA in $\text{Ru}_{\text{SA}}/\text{v-Mo}_2\text{C}$, which is coincident with the XPS analysis. The analysis on the first derivative curve further confirms the valence state of Ru SAs in $\text{Ru}_{\text{SA}}/\text{v-Mo}_2\text{C}$ to be +0.74.^[29] The isolated dispersion of Ru atoms in $\text{Ru}_{\text{SA}}/\text{v-Mo}_2\text{C}$ was proved by the Fourier-transformed (FT) extended X-ray absorption fine structure (FT-EXAFS) spectrum at the Ru K-edge, where no Ru–Ru bond but distinct peaks at 1.41 and 2.51 Å corresponding to the Ru–C/N bond with a coordination number of 4 and the Ru–Mo bond in the second coordination shell were distinguished (Figure 3e; and Figure S8 and Table S1, Supporting Information).^[30] This is further evidenced by the N K-edge XANES spectra, where the peak for π^* pyridinic of $\text{Ru}_{\text{SA}}/\text{v-Mo}_2\text{C}$ splits into π^{*1} pyridinic and π^{*2} pyridinic peaks compared to v- Mo_2C and Mo_2C , suggesting a portion of the pyridinic-N is bound to the Ru SA (Figure S9, Supporting Information).^[31] Moving to the Mo K-edge XANES spectrum of $\text{Ru}_{\text{SA}}/\text{v-Mo}_2\text{C}$, a more positive shift from Mo foil compared to v- Mo_2C was observed (Figure 3f), indicating a lower average electron density around Mo atoms in $\text{Ru}_{\text{SA}}/\text{v-Mo}_2\text{C}$ due to charge transfer from Mo_2C to Ru SAs. Additionally, v- Mo_2C exhibits a negative shift compared to Mo_2C , suggesting the presence of $\text{V}_{\text{Mo}}^{n+}$ defects in v- Mo_2C . In the Mo K-edge FT-EXAFS, two peaks at 1.50 and 2.60 Å are assigned to scattering features of Mo–C/N and Mo–Mo bonds in $\text{Ru}_{\text{SA}}/\text{v-Mo}_2\text{C}$ (Figure 3g; and Figures S10–S11 and Table S2, Supporting Information). Notably, the similar bond lengths of Mo–Mo and Ru–Mo in $\text{Ru}_{\text{SA}}/\text{v-Mo}_2\text{C}$ verify that the Ru SAs locate at the $\text{V}_{\text{Mo}}^{n+}$ sites, and the decreased Mo–Mo peak intensity of Ru/v- Mo_2C relative to v- Mo_2C is attributed to structural disorder resulting from atomic rearrangement after substitutional doping with isolated Ru SAs.^[32] These findings are further intuitively supported by the wavelet-transform (WT) of the Ru K-edge and Mo K-edge EXAFS oscillations of $\text{Ru}_{\text{SA}}/\text{v-Mo}_2\text{C}$ (Figure 3h,i). The above analyses unequivocally confirm that low-valence Ru SAs are dispersed within the Mo_2C lattice, inducing a strong metal–metal electronic interaction, which lays the foundation for ameliorating the intermediates adsorption kinetics in HER/HzOR electrocatalysis.

2.3. Electrocatalytic HER and HzOR Performances

The electrocatalytic HER performance of $\text{Ru}_{\text{SA}}/\text{v-Mo}_2\text{C}$ was investigated in alkaline 1 M KOH and 0.5 M H_2SO_4 aqueous solutions, respectively. In 1 M KOH, the linear sweep voltammetry (LSV) curves reveal that $\text{Ru}_{\text{SA}}/\text{v-Mo}_2\text{C}$ achieves a low overpotential of 27.5 mV to attain a current density of 10 mA cm⁻², which is markedly lower than those of v- Mo_2C (157 mV), $\text{Ru/Mo}_2\text{C}$ (104 mV), Mo_2C (147 mV), and also outperforms the commercial benchmark 20 wt% Pt/C (34.1 mV) (Figure 4a). The high intrinsic activity of $\text{Ru}_{\text{SA}}/\text{v-Mo}_2\text{C}$ is endorsed by a low Tafel slope of 35.8 mV dec⁻¹ and a high exchange current density (j_0) of 1.88 mA cm⁻², which are comparable to those of Pt/C (39.1 mV dec⁻¹ and

2.03 mA cm⁻²) (Figure 4b), signifying the Pt-like high catalytic efficacy of $\text{Ru}_{\text{SA}}/\text{v-Mo}_2\text{C}$ for HER following an ideal Volmer–Tafel mechanism. The superior reaction kinetics of $\text{Ru}_{\text{SA}}/\text{v-Mo}_2\text{C}$ is further affirmed by other derivative metrics including the lowest charge transfer resistance (R_{ct}), and the highest electrochemical active surface area (ECSA)-normalized current density (j_{ECSA}), mass-normalized current density (j_{Mass}), and turnover frequency (TOF) for H_2 generation per active site among the samples (Figures S12–S16 and Table S3, Supporting Information). Specifically, as shown in Figure 4c, $\text{Ru}_{\text{SA}}/\text{v-Mo}_2\text{C}$ exhibits much higher j_{ECSA} (0.34 mA cm⁻²) and j_{Mass} (0.42 A mg_{metal}⁻¹) than those of Pt/C (0.05 mA cm⁻² and 0.17 A mg_{metal}⁻¹) at an overpotential of 50 mV (η_{50}). In addition, the TOF of $\text{Ru}_{\text{SA}}/\text{v-Mo}_2\text{C}$ at η_{50} (0.22 s⁻¹) also surpasses that of Pt/C (0.17 s⁻¹), indicating its excellent intrinsic site-specific activity for HER. Of note, the remarkable alkaline HER performance of $\text{Ru}_{\text{SA}}/\text{v-Mo}_2\text{C}$ also outstrips overwhelming majority of the reported Mo-/Ru-based HER catalysts thus far (Table S4, Supporting Information).^[33] Moreover, in 0.5 M H_2SO_4 solution, $\text{Ru}_{\text{SA}}/\text{v-Mo}_2\text{C}$ also exhibits a commendable acidic HER activity, showcasing an overpotential of 36.5 mV at 10 mA cm⁻² and a low Tafel slope of 40.5 mV dec⁻¹ (Figure 4d,e). Corresponding denotative metrics likewise measured in 0.5 M H_2SO_4 again evidence its high intrinsic HER activity surpassing those of Ru/ Mo_2C , v- Mo_2C , and Mo_2C and closing to Pt/C (Figures S17–S21 and Table S5, Supporting Information). It is noteworthy that the anomalously inferior acidic HER activity compared to that in 1 M KOH may be reasoned to the presence of acid-resistant, while alkali-vulnerable MoO_x species on the catalysts surface, which pulls down the apparent activity of $\text{Ru}_{\text{SA}}/\text{v-Mo}_2\text{C}$ in the 0.5 M H_2SO_4 electrolyte. Importantly, $\text{Ru}_{\text{SA}}/\text{v-Mo}_2\text{C}$ demonstrates superior HER catalytic stability in both 1 M KOH and 0.5 M H_2SO_4 electrolytes, which can sustain at 10 mA cm⁻² for 120 h with imperceptible potential decay (Figure 4f), thus underpinning the promising practical applications of $\text{Ru}_{\text{SA}}/\text{v-Mo}_2\text{C}$ in electrochemical HER.

Subsequently, the electrocatalytic HzOR activity of $\text{Ru}_{\text{SA}}/\text{v-Mo}_2\text{C}$ was examined in 1 M KOH aqueous electrolyte containing 0.5 M N_2H_4 . Impressively, the LSV curves reveal that $\text{Ru}_{\text{SA}}/\text{v-Mo}_2\text{C}$ demands an ultralow potential of −74.5 mV to achieve a current density of 10 mA cm⁻², which is remarkably superior to Ru/ Mo_2C (459 mV), Mo_2C (382 mV), and commercial 20 wt% Pt/C (96.5 mV) (Figure 4g). While v- Mo_2C only displayed a limited current density below 2 mA cm⁻² even at 0.5 V, suggesting the key role of Ru SA in facilitating HzOR on $\text{Ru}_{\text{SA}}/\text{v-Mo}_2\text{C}$. Notably, for delivering a high current density of 100 mA cm⁻², a potential as low as 0.02 V is required for $\text{Ru}_{\text{SA}}/\text{v-Mo}_2\text{C}$. Moreover, Tafel analysis reveals a super-low Tafel slope of $\text{Ru}_{\text{SA}}/\text{v-Mo}_2\text{C}$ (23.3 mV dec⁻¹), significantly lower than those of Pt/C (47.6 mV dec⁻¹), Ru/ Mo_2C (363 mV dec⁻¹), v- Mo_2C (209 mV dec⁻¹), and Mo_2C (238 mV dec⁻¹), indicating the fastest HzOR kinetics on $\text{Ru}_{\text{SA}}/\text{v-Mo}_2\text{C}$ (Figure 4h). This superiority is also evident in other derived metrics including j_{ECSA} , j_{Mass} , and TOF (Figures S22–S24, Supporting Information). Besides, the chronopotentiometry test shows a sustained HzOR stability of $\text{Ru}_{\text{SA}}/\text{v-Mo}_2\text{C}$ at 10 mA cm⁻² over 120 h under the intermittent hydrazine replenishment (Figure S25, Supporting Information). These outstanding performances rank $\text{Ru}_{\text{SA}}/\text{v-Mo}_2\text{C}$ as one of the top HzOR catalysts ever reported (Table S6, Supporting Information). To better illustrate the energy-saving advantage of the kinetically favorable HzOR,

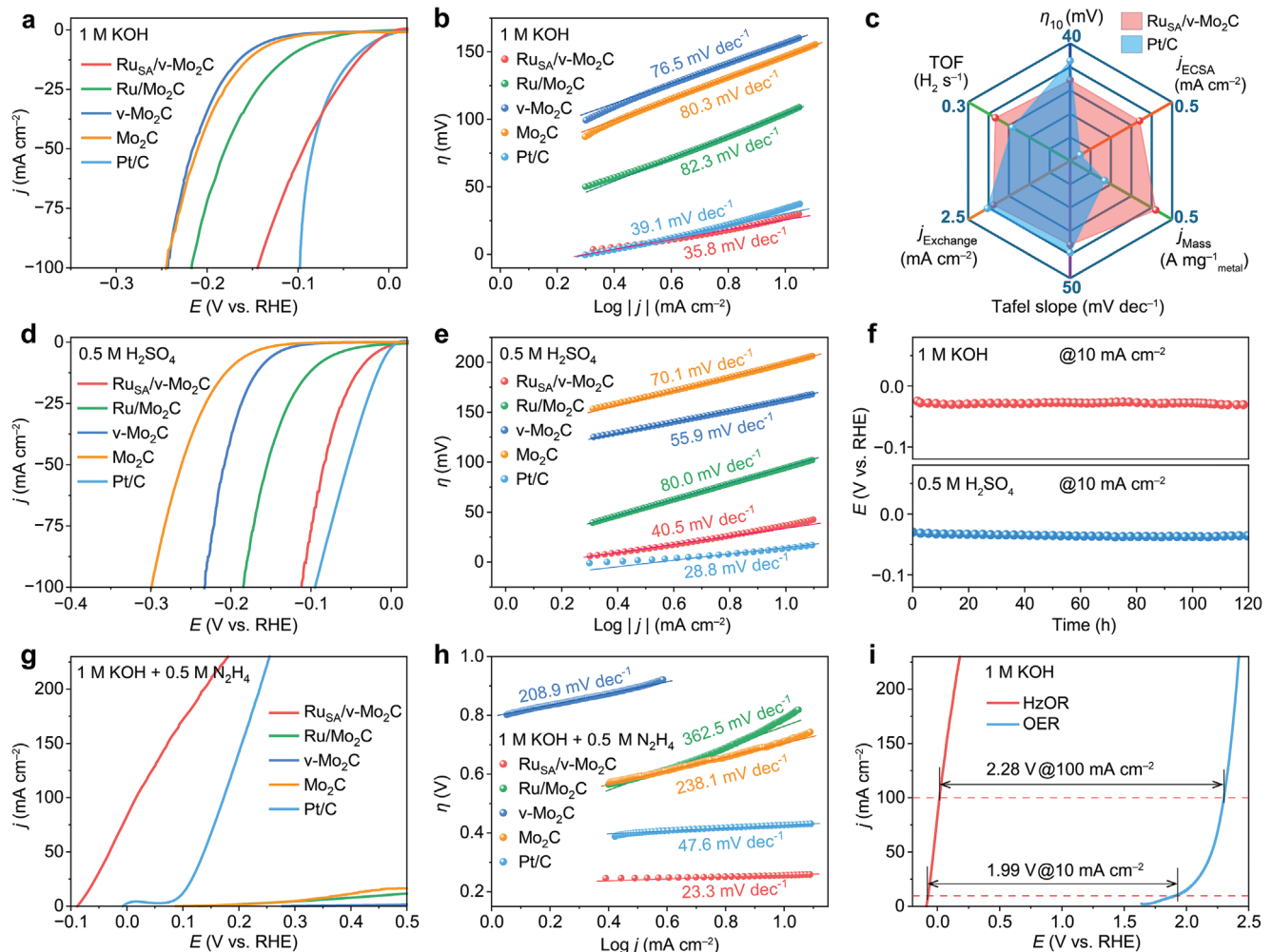


Figure 4. Electrocatalytic a–f) HER and g–i) HzOR performances of Ru_{SA}/v-Mo₂C, Ru/Mo₂C, v-Mo₂C, Mo₂C, and Pt/C. a) LSVs at 5 mV s⁻¹ and b) Tafel plots in 1 M KOH solution. c) Electrochemical metrics comparison between Ru_{SA}/v-Mo₂C and Pt/C in alkaline HER. d) LSVs at 5 mV s⁻¹ and e) Tafel plots in 0.5 M H₂SO₄ solution. f) Stability tests of Ru_{SA}/v-Mo₂C. g) LSVs at 5 mV s⁻¹ and h) Tafel plots in 1 M KOH solution containing 0.5 M N₂H₂. i) Comparison between HzOR and OER on Ru_{SA}/v-Mo₂C.

Figure 4i presents the comparison of HzOR (in 1 M KOH + 0.5 M N₂H₄) and OER (in 1 M KOH) on Ru_{SA}/v-Mo₂C. As observed, HzOR preceded OER with large potential gaps of 1.99 and 2.28 V at the current densities of 10 and 100 mA cm⁻², respectively, endorsing a significantly reduced energy consumption for H₂ production by coupling HzOR with HER.

2.4. Theoretical and In Situ Spectroscopic Studies

Density functional theory (DFT) calculations were performed to elucidate the underlying catalytic mechanism of Ru_{SA}/v-Mo₂C for both HER and HzOR. Figure 5a presents schematic models of Mo₂C (100) and Ru_{SA}/v-Mo₂C (100). The corresponding electron localization function (ELF) isosurface maps clearly indicate charge redistribution after introducing Ru single atom into Mo₂C matrix, with a net charge transfer of 0.055 e⁻ from Mo₂C to the Ru atom, strongly supporting the aforementioned XPS and XAFS analyses. The projected density of states (PDOS)

analysis shown in Figure 5b discloses a narrowed bandgap (E_g) and a downshifted d-band center (ϵ_d) for Ru_{SA}/v-Mo₂C compared to those of pristine Mo₂C, indicating enhanced electronic conductivity and improved intermediates desorption capabilities for Ru_{SA}/v-Mo₂C. The calculated Gibbs free energy profile for alkaline HER reveals that both the initial H₂O adsorption and the final H₂ desorption steps on pristine Mo₂C are endothermic, with the former having an energy barrier of 2.88 eV as the rate-determining step (RDS) (Figure 5c; and Figure S26, Supporting Information). Comparatively, both Ru and Mo sites in Ru_{SA}/v-Mo₂C render H₂O adsorption exothermic, and effectively lower the energy barrier for H₂ desorption, indicating ameliorated adsorption kinetics attributed to electronic coupling between Ru and Mo₂C. The HER free energy profiles of Ru and Mo sites in Ru_{SA}/v-Mo₂C exhibit similar trends, the disparity lies in that Ru site favors more for H₂O adsorption and subsequent dissociation, implying it is a more optimal place for the Volmer step. However, this benefit comes drawback of the difficult *OH desorption on Ru site (Figure S27, Supporting Information), which presents the

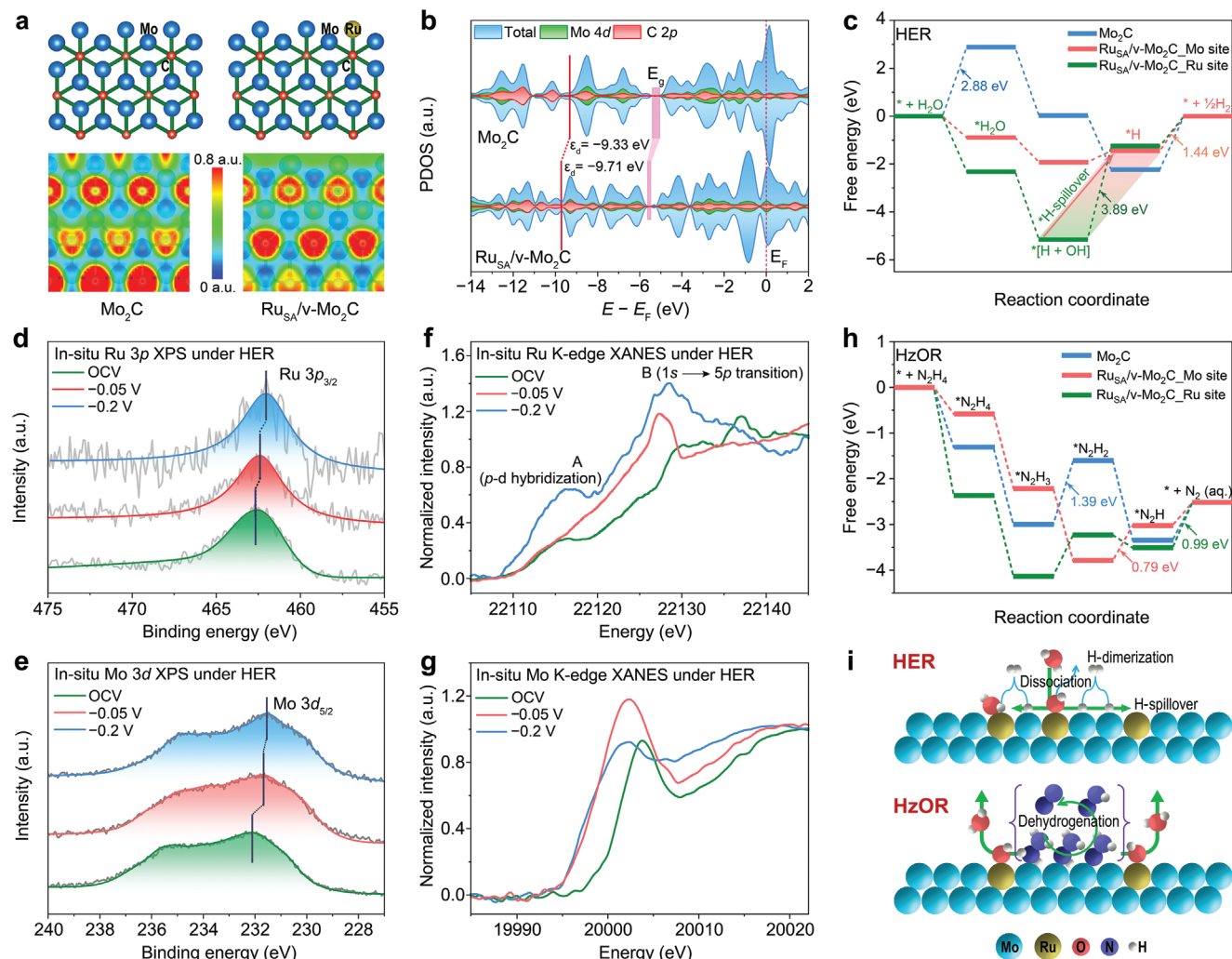


Figure 5. Theoretical and experimental insights into the catalytic mechanism. a) Structural models and ELF isosurface maps of Mo_2C and $\text{Ru}_{\text{SA}}/\text{v}-\text{Mo}_2\text{C}$. b) PDOS of Mo_2C and $\text{Ru}_{\text{SA}}/\text{v}-\text{Mo}_2\text{C}$. c) HER free energy profiles. d) Ru 3p and e) Mo 3d in situ NAP-XPS of $\text{Ru}_{\text{SA}}/\text{v}-\text{Mo}_2\text{C}$ under HER conditions. f) Ru K-edge and g) Mo K-edge in situ HERFD-XAS of $\text{Ru}_{\text{SA}}/\text{v}-\text{Mo}_2\text{C}$ under HER conditions. h) HzOR free energy profiles. i) Schematic catalytic mechanisms of HER and HzOR on $\text{Ru}_{\text{SA}}/\text{v}-\text{Mo}_2\text{C}$.

RDS with a significant energy barrier of 3.89 eV. In contrast, $^*\text{OH}$ desorption on Mo site is much easier, leading to a shift of the RDS to Heyrovsky/Tafel $^*\text{H}$ -combination step for H_2 desorption, with a small energy barrier of 1.44 eV. Figure S28 (Supporting Information) compares the Gibbs free energy changes (ΔG) concerning adsorbates ($^*\text{H}_2\text{O}$, $^*\text{H}$, and $^*\text{OH}$) on Mo_2C and the Mo and Ru sites of $\text{Ru}_{\text{SA}}/\text{v}-\text{Mo}_2\text{C}$. It is well perceived that an effective shortcut for HER on $\text{Ru}_{\text{SA}}/\text{v}-\text{Mo}_2\text{C}$ can be achieved through $^*\text{H}$ -spillover from Ru site to nearby Mo site, which facilitates streamlined reaction pathway and reduces overall energy barriers, thus rendering much superior activity over the pristine Mo_2C .

To support the above theoretical perspective, in situ attenuated total reflectance-surface-enhanced infrared absorption spectroscopy (ATR-SEIRAS) was performed during alkaline HER (Figure S29, Supporting Information). The spectra for both $\text{Ru}_{\text{SA}}/\text{v}-\text{Mo}_2\text{C}$ and $\text{v}-\text{Mo}_2\text{C}$ reveal several bands related to H_2O , including the O–H stretching vibration ($\nu_{\text{O}-\text{H}}$) in H_2O with different configurations spanning a broad range of 3000–3500 cm⁻¹,

the H–O–H bending vibration ($\delta_{\text{H}-\text{O}-\text{H}}$) at 1650 cm⁻¹, and the O–H bending vibration ($\delta_{\text{O}-\text{H}}$) at 1390 cm⁻¹.^[34] Compared to $\text{v}-\text{Mo}_2\text{C}$, the $\delta_{\text{H}-\text{O}-\text{H}}$ signal for $\text{Ru}_{\text{SA}}/\text{v}-\text{Mo}_2\text{C}$ is more distinct and exhibits a more pronounced enhancement as the applied potential decreased. Moreover, the peak of $\nu_{\text{O}-\text{H}}$ signal for $\text{Ru}_{\text{SA}}/\text{v}-\text{Mo}_2\text{C}$ displays a significant redshift to 3120 cm⁻¹, which can be attributed to the reorganization of hydrogen bond network of interfacial H_2O due to the strong OH binding at Ru and Mo sites in $\text{Ru}_{\text{SA}}/\text{v}-\text{Mo}_2\text{C}$.^[35] This is evidenced by the $\nu_{\text{Ru}-\text{OH}}$ and $\nu_{\text{Mo}-\text{OH}}$ signals observed at 1040 and 1183 cm⁻¹, respectively, both of which increased with decreasing potential. In contrast, only negligible $\nu_{\text{Mo}-\text{OH}}$ signal is detected on $\text{v}-\text{Mo}_2\text{C}$, and the $\delta_{\text{O}-\text{H}}$ is also absent. These observations clearly indicate that $\text{Ru}_{\text{SA}}/\text{v}-\text{Mo}_2\text{C}$ favors more for H_2O adsorption than $\text{v}-\text{Mo}_2\text{C}$. This conclusion is further corroborated by in situ Raman spectra, which reveals a more pronounced $\nu_{\text{O}-\text{H}}$ signal from adsorbed H_2O on $\text{Ru}_{\text{SA}}/\text{v}-\text{Mo}_2\text{C}$ than on $\text{v}-\text{Mo}_2\text{C}$ (Figure S30, Supporting Information).^[36] The $\nu_{\text{O}-\text{H}}$ Raman signal on $\text{Ru}_{\text{SA}}/\text{v}-\text{Mo}_2\text{C}$ remains stable as the

potential decreases, suggesting rapid removal of *H and OH^- on the active sites facilitated by a potential *H -spillover pathway. Besides, a new signal at 874 cm^{-1} is observed in the Raman spectra of $Ru_{SA}/v\text{-Mo}_2C$, which can be assigned to the ν_{Ru-H} signal according to previous recognitions.^[37] Notably, the ν_{Ru-H} signal exhibits a gradual enhancement with decreasing potential, indicating that the Ru sites in $Ru_{SA}/v\text{-Mo}_2C$ play a crucial role in both H_2O adsorption and the *H generation from H_2O dissociation. These experimental findings are in strong agreement with the theoretical results, providing a robust rationale for the hydrogen spillover mechanism from Ru sites to Mo sites, thereby facilitating the HER kinetics of $Ru_{SA}/v\text{-Mo}_2C$.

To provide evidence for the potential hydrogen spillover in $Ru_{SA}/v\text{-Mo}_2C$ during alkaline HER electrocatalysis, a series of comprehensive electrochemical experiments were performed. Initially, the hydrogen desorption kinetics of $Ru_{SA}/v\text{-Mo}_2C$, $v\text{-Mo}_2C$, and Pt/C were studied by in situ cyclic voltammetry (CV) in the double-layer region at various scan rates (Figure S31a–c, Supporting Information).^[38] The more positive hydrogen desorption peak potential observed for $Ru_{SA}/v\text{-Mo}_2C$ compared to Pt/C indicates a higher hydrogen binding energy (HBE) of $Ru_{SA}/v\text{-Mo}_2C$,^[39] which should be primarily attributed to the relatively strong Mo–H binding strength of the Mo_2C support, suggesting its capacity to capture the spillovered *H from Ru SAs. In stark contrast, $v\text{-Mo}_2C$ exhibits negligible hydrogen desorption peaks, which can be ascribed to its sluggish water dissociation kinetics and consequently limited *H generation. The plot of *H desorption peak position versus scan rate further reveals a much smaller slope of $Ru_{SA}/v\text{-Mo}_2C$ (4.5×10^{-5}) compared to Pt/C (2.83×10^{-4}) (Figure S31d, Supporting Information). This indicates a more rapid response of the *H desorption current to changes in the applied potential, implying the *H desorption kinetics of $Ru_{SA}/v\text{-Mo}_2C$ were accelerated by hydrogen spillover, in contrast to Pt/C with the absence of hydrogen spillover for HER. Such a hydrogen spillover-based HER pathway could be further supported by the pH-dependent relationship of HER on $Ru_{SA}/v\text{-Mo}_2C$, yielding a reaction order of 1.75, which is nearly double that of $v\text{-Mo}_2C$ (0.89) and approaches the theoretical value of 2, signifying a nearly uninhibited migration of *H (Figure S32, Supporting Information).^[40] Subsequently, the in situ electrochemical impedance spectroscopy (EIS) at various HER overpotentials were recorded and simulated using parallel equivalent circuit models to examine the hydrogen adsorption behavior (Figure S33, Supporting Information). In contrast to the relatively stable EIS of $v\text{-Mo}_2C$, both $Ru_{SA}/v\text{-Mo}_2C$ and Pt/C display a more pronounced response of charge transfer resistance as the overpotential varies from 0 to 40 mV, indicating their more remarkable hydrogen adsorption process (Figure S33a–c, Supporting Information). While compared to the relatively stable Bode plots of $v\text{-Mo}_2C$ and Pt/C at frequencies above 100 Hz, $Ru_{SA}/v\text{-Mo}_2C$ exhibits a continuously decreasing phase angle in the frequency range of 10–1000 Hz with increasing overpotential (Figure S33d–f, Supporting Information). This change suggests alterations at the electrolyte-electrocatalyst interface, which might be caused by the hydrogen spillover from Ru SAs to Mo_2C and the subsequent formation of Mo–H bonds. The decreased phase angle also indicates an enhanced capacitive behavior due to more electrons participate in the *H adsorption process.^[41] This can be further evidenced by the integration of hydrogen adsorp-

tion pseudocapacitance (C_ϕ) derived from equivalent circuit simulation versus overpotentials (Figure S33g, Supporting Information). The results reveal that $Ru_{SA}/v\text{-Mo}_2C$ exhibits over ten folds higher hydrogen adsorption charge (Q_{H^*}) (2478 μC) compared to $v\text{-Mo}_2C$ (234 μC), owing to a significantly enhanced hydrogen adsorption kinetics associated with the hydrogen spillover between Ru SAs and Mo_2C during HER (Figure S33h, Supporting Information). Furthermore, the EIS-derived Tafel slope was determined by plotting the hydrogen adsorption resistance (R_{H^*}) delivered by equivalent circuit simulation against the overpotential by virtue of the Ohm's law (Figure S33i, Supporting Information). Compared to Pt/C (33.88 mV dec $^{-1}$), $Ru_{SA}/v\text{-Mo}_2C$ exhibits a smaller Tafel slope of 21.32 mV dec $^{-1}$, aligning well with the theoretical value of 23 mV dec $^{-1}$ for a hydrogen spillover pathway.^[40] This finding strongly supports the involvement of hydrogen spillover mechanism in the HER electrocatalysis of $Ru_{SA}/v\text{-Mo}_2C$.

This HER duet performed by Ru and Mo sites of $Ru_{SA}/v\text{-Mo}_2C$ was further experimentally confirmed by in situ near-ambient pressure (NAP)-XPS at the Ru $3p_{3/2}$ and Mo $3d_{5/2}$ levels, in which both peaks exhibit a gradual redshift in binding energy as the voltage dropped from open-circuit voltage (OCV) to -0.05 V and then to -0.2 V , suggesting both Ru and Mo sites underwent a valence decrease and should play a role during HER (Figure 5d,e). Moreover, in situ high-energy-resolution fluorescence-detected (HERFD)-XANES spectra at both Ru and Mo K-edge further corroborated the gradual valence decrease with decreasing voltage during HER, along with significant changes in their local geometric structures (Figure 5f,g; and Figure S34, Supporting Information). At Ru K-edge, two well-resolved peaks denoted by pre-edge A and white-line B are observed at OCV, corresponding to the $4d-5p$ orbital hybridization and $1s \rightarrow 5p$ transition, respectively.^[42] The pre-edge peak A characterizes the local geometric configuration of Ru atom and is absent in the aforementioned ex-situ spectra, which can be rationalized by the favorable adsorption of OH^- in electrolyte. This peak becomes faint at -0.05 V due to likely removal of OH^- caused by electrostatic repulsion, and then recovers at -0.2 V , which can be ascribed to the substitutive H_2O adsorption under HER conditions, this enhanced $p-d$ hybridization also results in a heightened white line peak B. At Mo K-edge, the increased white line intensity as voltage moves from OCV to -0.05 V can be reasoned to an increased $5p$ states due to electrolyte OH^- removal. Conversely, the regressive white line intensity at -0.2 V is presumed to arise from the covalent interactions between Mo site and the adsorbed $\cdot H$ radical (*H), which breaks the degeneracy of $5p$ orbitals, leading to an elevation in $5p$ energy levels.^[43] These in situ spectral analyses endorse the theoretical findings that the HER on $Ru_{SA}/v\text{-Mo}_2C$ involves a synergistic cooperation of Ru and Mo sites, which are responsible for the Volmer and Heyrovsky/Tafel steps, respectively.

In addition, the HzOR free energy profile was also calculated (Figure 5h; and Figures S35–S37, Supporting Information). The results reveal that Mo_2C is thwarted by the largest energy barrier of 1.39 eV for RDS ($^*N_2H_3 \rightarrow ^*N_2H_2$). In contrast, the introduction of Ru not only alters the RDS but also reduces the RDS energy barriers to 0.99 and 0.79 eV on the Ru and Mo sites, respectively. Besides, the $^*N_2H_3 \rightarrow ^*N_2H_2$ dehydrogenation on Ru site still faces a considerable uphill free energy, while it occurs spontaneously on Mo site, highlighting the optimized electronic

structure caused by Ru incorporation, e.g., the downshifted ε_d . Given the high OH⁻ affinity and electron-withdrawing propensity of Ru site, it is highly likely that the electron-deficient Mo site serves as the primary active site for the nucleophilic attack of hydrazine. Meanwhile, the adjacent OH⁻-adsorbed Ru site could facilitate the *N-H dehydrogenation process by expediting H₂O formation. This dual-site synergy between Ru and Mo sites in HzOR was further experimentally substantiated by *in situ* Raman spectroscopy study (Figure S38, Supporting Information). The absence of the ν_{N-N} signal at 1233 cm⁻¹ in spectra of v-Mo₂C, compared to that of Ru_{SA}/v-Mo₂C, indicates a weaker adsorption for hydrazine on v-Mo₂C than on Ru_{SA}/v-Mo₂C.^[44] Additionally, both the ν_{N-H} and δ_{N-H} signals in the v-Mo₂C spectra remain almost unchanged with varying potentials, suggesting the lower HzOR activity of v-Mo₂C. In contrast, the ν_{N-H} , δ_{N-H} , and ν_{N-N} signals in the Ru_{SA}/v-Mo₂C spectra all exhibit significant attenuation as the potential increases, and the gradual blueshift of the ν_{N-H} signal can be attributed to the transition to ν_{O-H} signal at higher potentials, indicating rapid oxidation removal of hydrazine on Ru_{SA}/v-Mo₂C. Notably, the attenuation of ν_{N-H} , δ_{N-H} , and ν_{N-N} signals is accompanied by a synchronous reduction of the ν_{Ru-OH} signal at 1023 cm⁻¹. This observation provides compelling evidence that OH⁻ adsorbed on Ru sites facilitates the hydrazine oxidation process occurring on Mo sites. By gleaning these analyses, a schematic diagram is depicted to explicitly demonstrate the catalytic mechanisms of Ru_{SA}/v-Mo₂C for both HER and HzOR. As illustrated in Figure 5i, in HER, the Ru site promotes H₂O dissociation, pumping *H onto adjacent Mo site where it dimerizes into H₂. Whereas in HzOR, the Ru site adsorbs OH⁻, aiding in extracting proton from *N₂H_x intermediates to enhance the dehydrogenation kinetics. Thus, it is the synergistic duo of Ru and Mo sites dominates both reactions.

2.5. Self-Powered H₂ Production by Hydrazine–H₂O Battery

Motivated by the excellent bifunctionality of Ru_{SA}/v-Mo₂C toward HzOR and HER, we explored its potential for energy-saving H₂ production through electrocatalytic overall hydrazine splitting (OHzS) in a two-electrode H-type electrolyzer using 1 M KOH with and without 0.5 M N₂H₄ as anolyte and catholyte, respectively. Figure 6a illustrates a comparison of polarization curves for OHzS and overall water splitting (OWS), in which significantly enhanced energy efficiency can be intuitively seen when employing HzOR to assist H₂ production. Specifically, the OHzS cell demonstrated a remarkable capability to reach the current densities of 10 and 100 mA cm⁻² at impressively low voltages of 0.12 and 0.8 V, respectively, which are 1.95 and 2.17 V less than those required in OWS cell. In practice, this OHzS cell can be easily driven by a commercial cylindrical battery of 1.5 V, as illustrated in Figure 6b; and Movie S3 (Supporting Information). To be more intuitive, with a DC power supply at only 1.4 V, a large current density of 220 mA cm⁻² was delivered (Figure S39, Supporting Information). Noteworthily, both the HER and HzOR kinetics of Ru_{SA}/v-Mo₂C exhibited significant enhancement at an elevated temperature of 90 °C, leading to an intensified current output up to 400 mA cm⁻² at merely 0.6 V for the high-temperature OHzS cell (Figures S40–S42, Supporting Information). This impres-

sive performance exhibited by Ru_{SA}/v-Mo₂C for OHzS also ranks among the top results realized by bifunctional electrocatalysts including those self-supported on conductive substrates (Table S7, Supporting Information).

To exemplify the proof-of-principle self-powered H₂ production by OHzS with hydrazine as the sole consumable, a homemade prototype hydrazine–H₂O battery equipped with bifunctional Ru_{SA}/v-Mo₂C electrocatalyst and pump-circulated pH-asymmetric catholyte (0.5 M H₂SO₄, pH = 0.27) and anolyte (1 M KOH + 0.5 M N₂H₄, pH = 13.85) separated by a bipolar membrane was designed and constructed. The battery exhibits an actual high open-circuit voltage (OCV) of 1.366 V (Figure 6c), surpassing its theoretical value (1.16 V) probably due to the deviation from thermodynamic equilibrium conditions, and can stabilize up to 10000 s without any noticeable self-discharging. During discharging, the battery reaches a peak power density of 10.51 mW cm⁻² at a current density of 35 mA cm⁻² (Figure 6d). Moreover, it exhibits impressive rate performance across various discharging current densities (2–20 mA cm⁻²) over a duration of 1000 s, with an output voltage close to 0.6 V at 20 mA cm⁻², and the voltage can recover back to 0.78 V when the current density returned from 20 to 2 mA cm⁻² (Figure 6e). To further assess the energy density, a galvanostatic test at 10 mA cm⁻² in static electrolytes was conducted. As shown in Figure 6f, the battery sustained for ≈90 h until depletion of N₂H₄ occurred, delivering an astonishing energy density up to 358 Wh g_{N2H4}⁻¹. Furthermore, the reusability of this battery was confirmed by five consecutive galvanostatic cycles at 10 mA cm⁻² for 1 h with refreshed anolyte in each cycle, demonstrating consistent battery performance and excellent recovery capability (inset in Figure 6f).

To implement the conceived self-powered H₂ production system, the alkaline OHzS electrolytic cell was connected to the pH-decoupled hydrazine–H₂O battery (Figure 6g). Notably, upon cascading, substantial bubbles were immediately burst out from both electrodes surface (Movie S4, Supporting Information), and the generated H₂ was collected using the drainage method (Figure S43, Supporting Information). It is noteworthy that both the electrolytic cell and battery proceeded the OHzS reaction, hence H₂ from both sources were harvested, rendering a twofold increase in Faradaic efficiency for H₂ production compared to conventional water electrolysis. As illustrated in Figure 6h, a total of 1.8 mmol of H₂, including 0.9 mmol each from both the electrolytic cell and battery, was collected from this self-powered system after a 1 h run, corresponding to an amazing H₂ production rate of 18 mol h⁻¹ m⁻² (equivalent to 403.2 L h⁻¹ m⁻² at STP). This achieved rate surpasses all of the reported self-powered H₂ production systems, including the direct hydrazine–O₂/H₂O₂ fuel cells, sulfide fuel cells, Zn–polysulfides battery, Zn–polysulfides battery, and Mg–seawater battery (Figure 6i; and Table S8, Supporting Information).^[45] Given the absence of expenses on electricity, H₂ storage and transport, the H₂ production cost by this self-powered system is only from the Ru_{SA}/v-Mo₂C electrode (\$2.8 m⁻², based on the price of and loading of precious Ru). This cost structure aligns well with the 2025 target of 7 \$ kg_{H2}⁻¹ for the comprehensive cost of H₂ production, delivery, and dispensing set by the US Department of Energy (DOE). These findings strongly demonstrate that the proposed hydrazine–H₂O battery, in conjunction with the high-performance Ru_{SA}/v-Mo₂C catalyst, holds significant potential for both energy-/

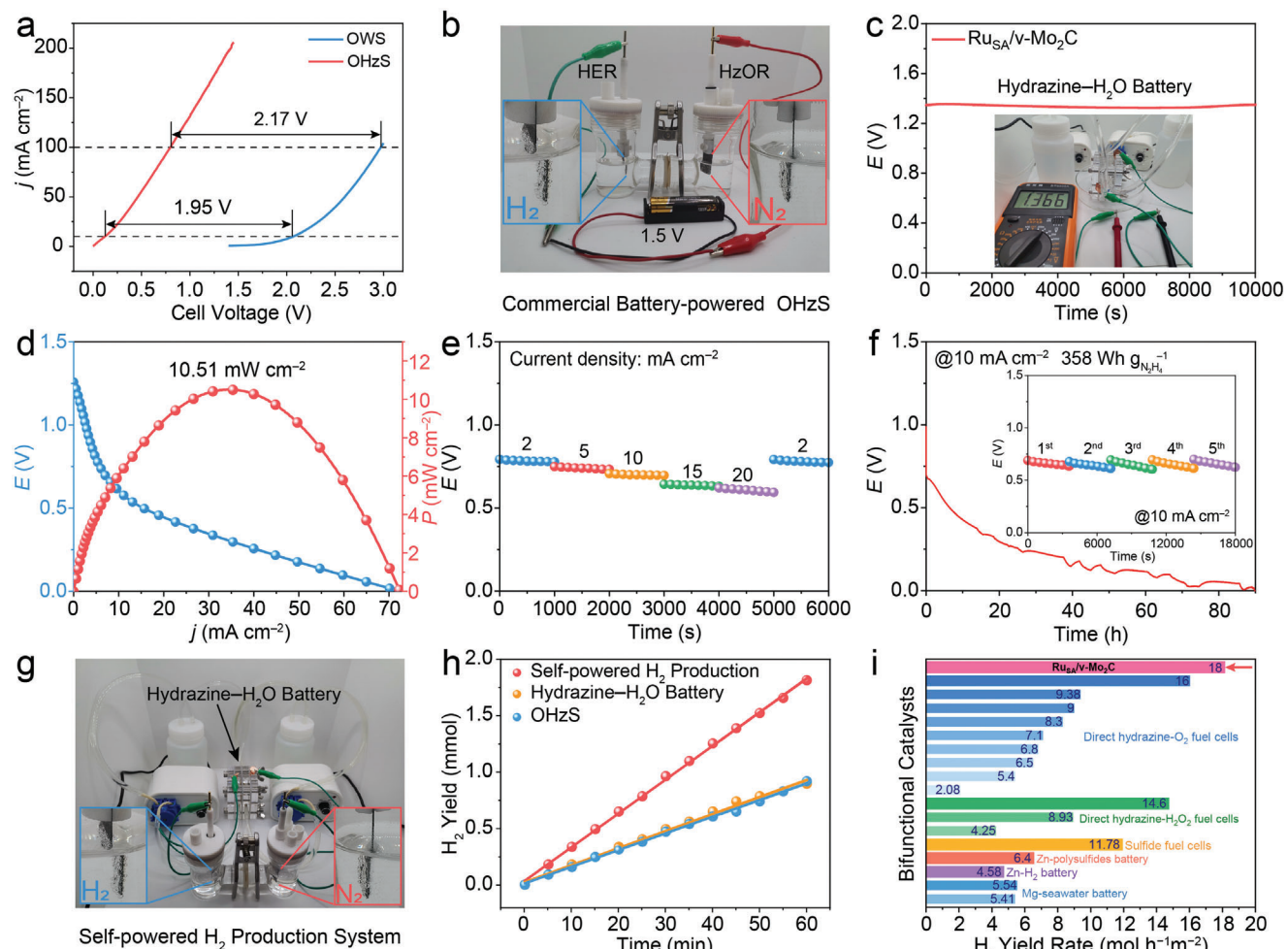


Figure 6. OHzS and hydrazine–H₂O battery performances. a) Comparison of OWS and OHzS on Ru_{SA}/v-Mo₂C || Ru_{SA}/v-Mo₂C electrode couple. b) Photo of Ru_{SA}/v-Mo₂C-catalyzed OHzS driven by a commercial cylindrical battery (1.5 V), insets show the bubbles produced on each electrode during the reaction. c) OCV–time plot of the hydrazine–H₂O battery, inset shows the measured instantaneous OCV. d) Discharging polarization and power density curves and e) voltage–time curves of the hydrazine–H₂O battery at different current densities. f) Prolonged voltage–time curve of the hydrazine–H₂O battery at a discharging current density of 10 mA cm⁻², inset shows five consecutive voltage–time tests. g) Photo demonstrating H₂ production via hydrazine splitting self-powered by the hydrazine–H₂O battery. h) Amounts of H₂ measured in the self-powered system over time. i) Comparison of H₂ production rate of the herein proposed system with other reported systems.

cost-efficient and scalable clean H₂ production as well as its flexible application scenarios.

3. Conclusion

Low-valence Ru single atoms electrocatalyst with a 4.14 wt% high loading on Mo₂C nanobelts (Ru_{SA}/v-Mo₂C) has been successfully synthesized via an efficient vacancy-trapping strategy. This catalyst demonstrates excellent alkaline/acidic-universal HER electrocatalytic performance in both 1 M KOH and 0.5 M H₂SO₄ electrolytes, which are superior and comparable to the benchmark Pt/C, respectively, while also maintaining robust long-term stability. Moreover, it exhibits an outstanding alkaline HzOR performance significantly exceeding that of Pt/C. Building on this superb bifunctionality, a fantastic hydrazine–H₂O battery with pH-decoupled electrolytes has been designed, which shows a high open circuit voltage up to 1.37 V and an energy den-

sity of 358 Wh kg_{N2H4}⁻¹. As a proof-of-concept, a genuine self-powered hydrazine splitting system for energy-saving H₂ production has been established by driving an alkaline hydrazine splitting electrolyzer with power from the hydrazine–H₂O battery. This system empowers a remarkable H₂ production rate of 18 mol h⁻¹ cm⁻² (i.e., 403.2 L h⁻¹ cm⁻² at STP) at a low cost, distinguishing it as one of the best ever reported H₂ production electrolyzers. Furthermore, DFT calculations and in situ spectroscopic studies collectively unveil a synergistic catalytic mechanism for Ru_{SA}/v-Mo₂C, i.e., the Ru single atoms respectively facilitate the H₂O dissociation and formation in HER and HzOR, thereby expediting the *H-combination and *N–H dehydrogenation steps on the Mo sites. The present study showcases an innovative single chemical-initiated battery design that will shed light on novel scenarios for energy-efficient and facile H₂ production guided by the principle of galvanic redox chemistry.

Supporting Information

Supporting Information is available from the Wiley Online Library or from the author.

Acknowledgements

This work was supported by the National Key Research and Development Program of China (No. 2022YFA1505700), National Natural Science Foundation of China (Nos. 22475214, 22205232, 22222801, and 21601187), Talent Plan of Shanghai Branch, Chinese Academy of Sciences (No. CASSHB-QNPD-2023-020), Natural Science Foundation of Fujian Province (Nos. 2023J06044 and 2023J01213), and the Self-deployment Project of Haixi Institutes, Chinese Academy of Sciences (Nos. CXZX-2022-JQ06 and CXZX-2022-GH03). The synchrotron studies on beamlines TPS 44A and TLS 24A1 at National Synchrotron Radiation Research Center (NSRRC), and beamline BL12XU at SPring-8 (Japan) are highly acknowledged. The authors also greatly appreciate support by Transmission Electron Microscope Platform and High-performance Computing Platform of Fujian Science & Technology Innovation Laboratory for Optoelectronic Information of China.

Conflict of Interest

The authors declare no conflict of interest.

Data Availability Statement

The data that support the findings of this study are available from the corresponding author upon reasonable request.

Keywords

electrocatalysis, energy conversion, hydrogen evolution, hydrazine oxidation, self-powered

Received: October 22, 2024

Revised: December 14, 2024

Published online: January 2, 2025

- [1] X. Yang, C. P. Nielsen, S. Song, M. B. McElroy, *Nat. Energy* **2022**, *7*, 955.
- [2] Z. Yan, J. L. Hitt, J. A. Turner, T. E. Mallouk, *Proc. Natl. Acad. Sci. USA* **2020**, *117*, 12558.
- [3] a) M. Chatenet, B. G. Pollet, D. R. Dekel, F. Dionigi, J. Deseure, P. Millet, R. D. Braatz, M. Z. Bazant, M. Eikerling, I. Staffell, P. Balcombe, Y. Shao-Horn, H. Schäfer, *Chem. Soc. Rev.* **2022**, *51*, 4583; b) Z. Zhuang, Y. Wang, C.-Q. Xu, S. Liu, C. Chen, Q. Peng, Z. Zhuang, H. Xiao, Y. Pan, S. Lu, R. Yu, W.-C. Cheong, X. Cao, K. Wu, K. Sun, Y. Wang, D. Wang, J. Li, Y. Li, *Nat. Commun.* **2019**, *10*, 4875.
- [4] Z. P. Ifkovits, J. M. Evans, M. C. Meier, K. M. Papadantonakis, N. S. Lewis, *Energy Environ. Sci.* **2021**, *14*, 4740.
- [5] S. S. Garud, F. Tsang, I. A. Karimi, S. Farooq, *Energy Convers. Manage.* **2023**, *286*, 117059.
- [6] a) J.-T. Ren, L. Chen, H.-Y. Wang, W.-W. Tian, Z.-Y. Yuan, *Energy Environ. Sci.* **2024**, *17*, 49; b) Q. Qian, Y. Zhu, N. Ahmad, Y. Feng, H. Zhang, M. Cheng, H. Liu, C. Xiao, G. Zhang, Y. Xie, *Adv. Mater.* **2024**, *36*, 2306108.
- [7] a) H. Liu, Y. Liu, M. Li, X. Liu, J. Luo, *Mater. Today Adv.* **2020**, *7*, 100083; b) T. Y. Burshtein, Y. Yasman, L. Muñoz-Moene, J. H. Zagal, D. Eisenberg, *ACS Catal.* **2024**, *14*, 2264.
- [8] X. Zhai, Q. Yu, J. Chi, X. Wang, B. Li, B. Yang, Z. Li, J. Lai, L. Wang, *Nano Energy* **2023**, *105*, 108008.
- [9] a) X. Liu, J. He, S. Zhao, Y. Liu, Z. Zhao, J. Luo, G. Hu, X. Sun, Y. Ding, *Nat. Commun.* **2018**, *9*, 4365; b) Y. Liu, J. Zhang, Y. Li, Q. Qian, Z. Li, Y. Zhu, G. Zhang, *Nat. Commun.* **2020**, *11*, 1853; c) Y. Hu, T. Chao, Y. Li, P. Liu, T. Zhao, G. Yu, C. Chen, X. Liang, H. Jin, S. Niu, W. Chen, D. Wang, Y. Li, *Angew. Chem., Int. Ed.* **2023**, *62*, 202308800; d) L. Zhu, J. Huang, G. Meng, T. Wu, C. Chen, H. Tian, Y. Chen, F. Kong, Z. Chang, X. Cui, J. Shi, *Nat. Commun.* **2023**, *14*, 1997.
- [10] W. Zhu, X. Zhang, F. Yao, R. Huang, Y. Chen, C. Chen, J. Fei, Y. Chen, Z. Wang, H. Liang, *Angew. Chem., Int. Ed.* **2023**, *62*, 202300390.
- [11] a) J. Li, Y. Li, J. Wang, C. Zhang, H. Ma, C. Zhu, D. Fan, Z. Guo, M. Xu, Y. Wang, H. Ma, *Adv. Funct. Mater.* **2022**, *32*, 2109439; b) Y. Kuang, F. Yang, L. Feng, *Adv. Energy Mater.* **2024**, *14*, 2402043.
- [12] H. Fang, D. Liu, Y. Luo, Y. Zhou, S. Liang, X. Wang, B. Lin, L. Jiang, *ACS Catal.* **2022**, *12*, 3938.
- [13] L. Hou, X. Gu, X. Cui, J. Tang, Z. Li, X. Liu, J. Cho, *EES Catal.* **2023**, *1*, 619.
- [14] a) S. Zuo, W. Xue, Y. Zhang, J. Chen, Z. Lin, *ChemNanoMat* **2024**, *10*, 202300476; b) Z. Li, Y. Yan, M. Liu, Z. Qu, Y. Yue, T. Mao, S. Zhao, M. Liu, Z. Lin, *Proc. Natl. Acad. Sci. USA* **2023**, *120*, 2218261120; c) W. Xue, Q. Zhou, X. Cui, J. Zhang, S. Zuo, F. Mo, J. Jiang, X. Zhu, Z. Lin, *Angew. Chem., Int. Ed.* **2023**, *62*, 202307504.
- [15] W. Chen, M. Yu, S. Liu, C. Zhang, S. Jiang, G. Duan, *Adv. Funct. Mater.* **2024**, *34*, 2313307.
- [16] Y. Deng, Y. Ge, M. Xu, Q. Yu, D. Xiao, S. Yao, D. Ma, *Acc. Chem. Res.* **2019**, *52*, 3372.
- [17] J. Zhang, L. Zhang, J. Liu, C. Zhong, Y. Tu, P. Li, L. Du, S. Chen, Z. Cui, *Nat. Commun.* **2022**, *13*, 5497.
- [18] a) R. Vasant Kumar, T. Sarakonsri, *Rechargeable Ion Batteries*, Wiley, New York **2023**, pp. 1–20; b) S.-j. Xie, C.-H. Zhen, H.-w. Chen, D.-q. Cao, J. Zhang, Y. Zhou, J.-T. Li, S.-G. Sun, *J. Phys. Chem. C* **2022**, *126*, 17002.
- [19] L. Zhang, X. Wang, R. Wang, M. Hong, *Chem. Mater.* **2015**, *27*, 7610.
- [20] L. Zhang, N. Jin, Y. Yang, X.-Y. Miao, H. Wang, J. Luo, L. Han, *Nano-Micro Lett.* **2023**, *15*, 228.
- [21] Y. Yang, Y. Qian, Z. Luo, H. Li, L. Chen, X. Cao, S. Wei, B. Zhou, Z. Zhang, S. Chen, W. Yan, J. Dong, L. Song, W. Zhang, R. Feng, J. Zhou, K. Du, X. Li, X.-M. Zhang, X. Fan, *Nat. Commun.* **2022**, *13*, 7225.
- [22] a) X. Liu, H. Xu, F. Xie, C. Fasel, X. Yin, R. Riedel, *Carbon* **2020**, *163*, 254; b) S. Upadhyay, O. P. Pandey, *J. Power Sources* **2022**, *535*, 231450.
- [23] R. S. Armstrong, W. A. Horsfield, K. W. Nugent, *Inorg. Chem.* **1990**, *29*, 4551.
- [24] a) P. Su, W. Pei, X. Wang, Y. Ma, Q. Jiang, J. Liang, S. Zhou, J. Zhao, J. Liu, G. Q. Lu, *Angew. Chem., Int. Ed.* **2021**, *60*, 16044; b) X. Zhang, L. Xia, G. Zhao, B. Zhang, Y. Chen, J. Chen, M. Gao, Y. Jiang, Y. Liu, H. Pan, W. Sun, *Adv. Mater.* **2023**, *35*, 2208821.
- [25] a) C. Li, Z. Wang, M. Liu, E. Wang, B. Wang, L. Xu, K. Jiang, S. Fan, Y. Sun, J. Li, K. Liu, *Nat. Commun.* **2022**, *13*, 3338; b) T. Gu, R. Sa, L. Zhang, F. Zhou, R. Wang, X. Li, *J. Mater. Chem. A* **2020**, *8*, 20429.
- [26] Q. Gao, W. Zhang, Z. Shi, L. Yang, Y. Tang, *Adv. Mater.* **2019**, *31*, 1802880.
- [27] a) Y. Yang, Y. Xiao, L. Zhang, H.-T. Wang, K.-H. Chen, W.-X. Lin, N. Jin, C. Sun, Y.-C. Shao, J.-L. Chen, J. Qian, L. Han, *Appl. Catal., B* **2024**, *347*, 123792; b) H. Guan, W. Yi, T. Li, Y. Li, J. Li, H. Bai, G. Xi, *Nat. Commun.* **2020**, *11*, 3889.
- [28] a) K. Park, K. R. Lee, S. Ahn, C. V. Nguyen, K.-D. Jung, *Appl. Catal., B* **2024**, *346*, 123751; b) R. Vinoth, S. G. Babu, V. Bharti, V. Gupta, M. Navaneethan, S. V. Bhat, C. Muthamizhchelvan, P. C. Ramamurthy, C. Sharma, D. K. Aswal, Y. Hayakawa, B. Neppolian, *Sci. Rep.* **2017**, *7*, 43133.
- [29] a) J. Pei, L. Yang, J. Lin, Z. Zhang, Z. Sun, D. Wang, W. Chen, *Angew. Chem., Int. Ed.* **2024**, *63*, 202316123; b) L. Wang, Z. Xu, C.-H. Kuo, J.

- Peng, F. Hu, L. Li, H.-Y. Chen, J. Wang, S. Peng, *Angew. Chem., Int. Ed.* **2023**, *62*, 202311937.
- [30] Y. Zhang, Q. Wang, S. Yang, H. Wang, D. Rao, T. Chen, G. Wang, J. Lu, J. Zhu, S. Wei, X. Zheng, J. Zeng, *Adv. Funct. Mater.* **2022**, *32*, 2112452.
- [31] a) X. Wang, W. Chen, L. Zhang, T. Yao, W. Liu, Y. Lin, H. Ju, J. Dong, L. Zheng, W. Yan, X. Zheng, Z. Li, X. Wang, J. Yang, D. He, Y. Wang, Z. Deng, Y. Wu, Y. Li, *J. Am. Chem. Soc.* **2017**, *139*, 9419; b) J. Li, M. Li, N. An, S. Zhang, Q. Song, Y. Yang, X. Liu, *Proc. Natl. Acad. Sci. USA* **2021**, *118*, 2105628118.
- [32] K. Jiang, M. Luo, Z. Liu, M. Peng, D. Chen, Y.-R. Lu, T.-S. Chan, F. M. F. de Groot, Y. Tan, *Nat. Commun.* **2021**, *12*, 1687.
- [33] a) X. Cao, J. Huo, L. Li, J. Qu, Y. Zhao, W. Chen, C. Liu, H. Liu, G. Wang, *Adv. Energy Mater.* **2022**, *12*, 2202119; b) J. Li, J. Li, J. Hu, P. Chen, *Energy Fuels* **2023**, *37*, 17803.
- [34] J. Zhao, M. Kou, Q. Yuan, Y. Yuan, J. Zhao, *Small* **2024**, 2406022.
- [35] L. Zhang, H. Hu, C. Sun, D. Xiao, H.-T. Wang, Y. Xiao, S. Zhao, K. H. Chen, W.-X. Lin, Y.-C. Shao, X. Wang, C.-W. Pao, L. Han, *Nat. Commun.* **2024**, *15*, 7179.
- [36] J. Yin, T. Lu, J. Li, J. Liu, Y. Lin, D. Sun, L. Xu, Q. Zhao, H. Pang, S. Zhang, Y. Tang, *Adv. Funct. Mater.* **2024**, 2417034.
- [37] a) H. Zhang, K. Song, Z. Lin, Z. Wang, L. Zhang, S. Shen, L. Gu, W. Zhong, *Adv. Funct. Mater.* **2024**, *34*, 2405897; b) H. Fu, S. Lu, Y. Xin, S. Xiao, L. Chen, Y. Li, K. Shen, *Energy Environ. Sci.* **2025**.
- [38] J. Dai, Y. Zhu, Y. Chen, X. Wen, M. Long, X. Wu, Z. Hu, D. Guan, X. Wang, C. Zhou, Q. Lin, Y. Sun, S.-C. Weng, H. Wang, W. Zhou, Z. Shao, *Nat. Commun.* **2022**, *13*, 1189.
- [39] Q. Hu, K. Gao, X. Wang, H. Zheng, J. Cao, L. Mi, Q. Huo, H. Yang, J. Liu, C. He, *Nat. Commun.* **2022**, *13*, 3958.
- [40] J. Li, J. Hu, M. Zhang, W. Gou, S. Zhang, Z. Chen, Y. Qu, Y. Ma, *Nat. Commun.* **2021**, *12*, 3502.
- [41] Y. Hao, S.-F. Hung, C. Tian, L. Wang, Y.-Y. Chen, S. Zhao, K.-S. Peng, C. Zhang, Y. Zhang, C.-H. Kuo, H.-Y. Chen, S. Peng, *Angew. Chem., Int. Ed.* **2024**, *63*, 202402018.
- [42] W. Ziyu, N. L. Saini, S. Agrestini, D. D. Castro, A. Bianconi, A. Marcelli, M. Battisti, D. Gozzi, G. Balducci, *J. Phys. Condens. Matter* **2000**, *12*, 6971.
- [43] M. L. Baker, M. W. Mara, J. J. Yan, K. O. Hodgson, B. Hedman, E. I. Solomon, *Coord. Chem. Rev.* **2017**, *345*, 182.
- [44] P. Song, H. Wang, X. Cao, N. Liu, Q. Wang, R. Wang, *ChemElectroChem* **2020**, *7*, 212.
- [45] a) F. Sun, J. Qin, Z. Wang, M. Yu, X. Wu, X. Sun, J. Qiu, *Nat. Commun.* **2021**, *12*, 4182; b) B. Wang, X. Xiao, J. Li, M. Zhang, M. Jiao, Z. Zheng, T. Li, Q. Zhang, X. Zhang, G. Zhou, *Proc. Natl. Acad. Sci. USA* **2023**, *120*, 2317174120; c) J.-T. Ren, L. Chen, H.-Y. Wang, W. Tian, L. Wang, M. Sun, Y. Feng, S.-X. Zhai, Z.-Y. Yuan, *ACS Nano* **2023**, *17*, 25707; d) J. Chi, L. Guo, J. Mao, T. Cui, J. Zhu, Y. Xia, J. Lai, L. Wang, *Adv. Funct. Mater.* **2023**, *33*, 2300625.